HHS Public Access

Author manuscript

Nanomedicine (Lond). Author manuscript; available in PMC 2016 March 01.

Published in final edited form as:

Nanomedicine (Lond). 2015 March ; 10(4): 573–587. doi:10.2217/nnm.14.141.

Targeted Nanodiamonds as Phenotype Specific Photoacoustic Contrast Agents for Breast Cancer

Ti Zhang[1], **Huizhong Cui**[2], **Chia-Yi Fang**[3], **Kun Cheng**[4], **Xinmai Yang**[2], **Huan-Cheng Chang**[3], and **M. Laird Forrest**[1,**]

[1]Department of Pharmaceutical Chemistry, the University of Kansas, Lawrence, KS, 66047, USA

[2]Department of Mechanical Engineering, Bioengineering Research Center, the University of Kansas, Lawrence, KS, 66045, USA

[3]Institute of Atomic and Molecular Science, Academia Sinica, Taipei, 10617, Taiwan

[4]Division of Pharmaceutical Science, School of Pharmacy, the University of Missouri-Kansas City, Kansas City, MO, 64108, USA

Abstract

Aim—The aim is to develop irradiated nanodiamonds (INDs) as a molecularly-targeted contrast agent for high resolution and phenotype-specific detection of breast cancer with photoacoustic (PA) imaging.

Materials & Methods—The surface of acid treated radiation-damaged nanodiamonds was grafted with polyethylene glycol (PEG) to improve its stability and circulation time in blood, followed by conjugation to an anti-Human epidermal growth factor receptor-2 (HER2) peptide (KCCYSL) with a final nanoparticle size of *ca.* 92 nm. Immunocompetent mice bearing orthotopic HER2 positive or negative tumors were administered INDs and PA imaged using an 820-nm near infrared laser.

Results—PA images demonstrated that INDs accumulate in tumors and completely delineated the entire tumor within 10 hours. HER2 targeting significantly enhanced imaging of HER2-positive tumors. Pathological examination demonstrated INDs are non-toxic.

Conclusions—PA technology is adaptable to low-cost bedside medicine, and with new contrast agents described herein, PA can achieve high resolution (sub-mm) and phenotype specific monitoring of cancer growth.

Keywords

Nanodiamond; Photoacoustic Imaging; contrast agent; Breast Cancer; HER2

1. Introduction

Breast cancer is a leading cause of death in women, and 12% of the world's women will develop breast cancer in their lifetimes, although great progress in screening and treatment

**Author for correspondence: Phone: (785)864-4388, fax: (785)864-5736, mforrest@ku.edu.

has been made in recent decades [1]. In approximately 25% to 30% human breast cancers, human epidermal growth factor receptor 2 (HER2) is overexpressed on the surface of the tumor cells. HER2-positive breast cancers progress rapidly, and these patients have a poor prognosis and lower overall survival if untreated [2]. Therefore, there is a great need to develop effective diagnostic techniques for early detection of HER2-positive tumors.

Photoacoustic (PA) imaging is an emerging non-invasive and non-ionizing biomedical imaging modality that combines the high spatial resolution of ultrasound techniques and the excellent contrast of optical imaging with the help of various contrast agents [3–5]. Within the photoacoustic effect, light is absorbed by either the tissue or exogenous agents in the tissue and converted to ultrasound energy via transient thermal elastic expansion. The attenuation of acoustic energy is 1000 times weaker than that of light in biological tissues, thus PA imaging has a greater penetration depth of up to several centimeters compared to 1–2 mm for optical imaging techniques [6–9]. PA can image blood vessels, hemoglobin oxygenation and tumor angiogenesis with high contrast using the unique absorption spectra of endogenous hemoglobin and melanin [10–13]. The utilization of exogenous contrast agents has greatly enhanced PA imaging sensitivity and specificity, which are intrinsic disadvantages of traditional biomedical imaging modalities, such as computed tomography (CT) and ultrasound (UT) [14–17]. Organic dyes, quantum dots (QDs) and plasmonic nanoparticles have been used as contrast agents in PA imaging. Among these, contrast agents having high optical absorbance in the near-infrared (NIR) region are more attractive since the PA signal contribution from normal tissue and hemoglobin is minimum and the Mie scattering effect is relatively weak at wavelengths between 700 and 1100 nm. In addition to strong absorption in the NIR range, other properties of contrast agents that must be considered include toxicity, size, stability and surface chemistry. Some biocompatible dyes, including methylene blue and indocyanine green, have been used in PA imaging [18]. However, low molecular weight organic dyes are both non-specific in their localizations and are rapidly cleared from the plasma by the renal system, and fluorescent agents suffer from blinking and photobleaching which limit their clinical application, even though conjugation to nanoparticles can render them a suitable size for passive tumor uptake and retention. Plasmonic nanoparticles are the most developed PA contrast agents due to their tunable absorption and much stronger optical absorption than dyes based on the surface plasmon resonance (SPR) effect. Gold nanorods are used extensively in PA imaging because of their relatively simple synthesis, very strong SPR absorption in the NIR range, and ease of surface functionalization for the addition of targeting ligands [19, 20]. However, gold nanorods or nanobones melt and thus deform under intense laser light irradation. Although this strategy has been used to release DNA oligonucleotides and drugs [21, 22], gold nanoparticles do not provide a consistant and stable PA signal at a specific wavelength during the whole imaging process. In addition, the long-term toxicity of gold nanoparticles has to be considered in further human applications [23].

Owing to the excellent biocompatibility and exceptional optical stability, nanodiamonds (NDs) are an outstanding optical contrast agent and drug carrier for biomedical applications [24]. By introducing nitrogen vacancy centers as a fluorophor in the NDs, fluorescent nanodiamonds (FNDs) exhibit competitive advantages over organic fluorescent dyes and

QDs due to the long-term stability and low toxicity as an *in vivo* contrast agent [25–27]. Recently, alternative strategies for using nanodiamonds as imaging contrast agents have emerged. By making use of the detectable electron spin resonance of nitrogen-vacancy centers, different shapes of nanodiamond targets within chicken breast tissues were imaged with a spatial resolution of *ca.* 800 μm [28]. Carbon-dots (CDs) with tunable and strong photoluminescence produced by hydrothermal oxidation of nanodiamonds have been utilized for cell imaging [29]. Fabrication of nanodiamonds with a diethylenetriaminepentaacetic acid (DTPA) - Gadolinium chelate improved the signal intensity on T1-weighted magnetic resonance images [30].

In this work, a HER2 targeting moiety was conjugated to irradiated PEGylated NDs (PEG-INDs) to enhance the PA imaging sensitivity and contrast of HER2-overexpressing breast tumors. The HER2 receptor has been employed in pre-clinical research and the clinic as a molecular target for breast cancer drug delivery, tumor imaging and anticancer therapy [31–34]. However, the large size, limited stability and costs of antibodies limit the use for nanoparticle targeting. As a result, a six-amino acid peptide (KCCYSL) that targets HER2 was identified using phage display technology. Peptide conjugates offer the benefits of simplified production, flexible conjugation on terminals and enhanced cell permeability [35–37]. PA imaging combined with targeted INDs can provide high contrast of HER-positive tumors for identification of tumor growth and margins.

2. Materials and methods

2.1 Materials and Chemicals

N-(3-Dimethylaminopropyl)-N′-ethylcarbodiimide hydrochloride (EDC•HCl), N-Hydroxysuccinimide (NHS), sodium borate, sodium hydroxide, ethylenediamine tetraacetic acid (EDTA), adenosine 5′-diphosphate (ADP) sodium salt and potassium chloride (KCl) were purchased from Sigma-Aldrich (St. Louis, MO). Amine-PEG2000-amine was purchased from Jenkem Technology (Allen, TX). Fetal bovine serum (FBS) was purchased from Fisher Scientific (Pittsbrugh, PA). Dulbecco's Modified Eagle's Medium (DMEM) was purchased from Lonza (Allendale, NJ). Anti-Human epidermal growth factor receptor 2 (anti-HER2) peptide (KCCYSL) was synthesized by conventional means [36]. 4T1.2-neu murine cancer cells were provided by Dr. Zhaoyang You (University of Pittsburgh, Pittsburgh, PA). 4T1.2 breast cancer cells were provided by Dr. Beth A. Vorderstrasse (Washington State University, Pullman, WA) and used with the permission of the Peter MacCallum Cancer Centre (East Melbourne, Australia). Deionized (DI) water was used for preparing all of the solutions.

2.2 Synthesis and Characterization

Natural diamond powders (type Ia) with a median size of 0.125 μm were obtained from Microdiamant (NAT 0–0.25). They were grounded mechanically in a tungsten carbide (WC) vial containing 5 WC balls (10 mm in diameter) and mounted on a high-energy shaker mill (8000M, SPEX) for 45 min. Particles in the size range of 35 nm were extracted by centrifugation from the ball-milled diamonds after cleaning in mixed aqua regia-hydrogen peroxide solution (1:19, v/v) gently heated to 85 °C for 1 hr, followed by extensive washes

with DI water [38]. The extracted 35-nm NDs were then irradiated with 40-keV He^+ at a dose of ca. 3×10^{15} ions/cm^2 [39]. After purification in concentrated H_2SO_4-HNO_3 (3:1, v/v) at 100 °C in a microwave reactor for 3 hr, the He^+-irradiated NDs (or called INDs) were thoroughly washed with DI water and stored at room temperature before use.

The conjugation of amine-PEG-amine and anti-HER2 peptide with INDs followed a standard carbodiimide-mediated coupling procedure [40, 41]. Briefly, 2 mg of INDs were dissolved in 2 mL of sodium borate buffer (10 mM, pH 8.5), followed by sonication (Sonicator FS110, Fisher Scientific) for 30 min. EDC•HCl (4 mg) and NHS (4 mg) were added to the IND solution, which was stirred at room temperature (*ca.* 20 °C) for 0.5 hr to form the amine-reactive IND intermediates prior to addition of a 0.5-mL solution of amine-PEG2000-amine (10 mg). After stirring overnight, the amine-PEG-INDs were purified by centrifugation at 10,000 × g for 5 min, and the precipitate was washed three times with DI water. To synthesize the HER2-PEG-INDs, the carboxyl terminus of the anti-HER2 peptide (1 mg) was pre-activated by mixing with EDC•HCl (4 mg) and NHS (4 mg) for 0.5 hr in DI water, followed by addition of the amine-PEG-IND (2 mg) aqueous solution. The mixture was stirred for 18 hr and the resulting nanoparticles were separated from the solution by centrifugation, washed with DI water three times, and dried in a SpeedVap (Labconco).

Characteristic peaks in Fourier-transform infrared spectra (IRAffinity-1 FTIR Spectrophotometer, Shimazu) confirmed the coating of PEG and anti-HER2 peptide on the INDs. Hydrodynamic diameters and zeta potentials of IND particles in aqueous solution were determined using a ZetaPALS (Brookhaven Instrument Corporation). All measurements were carried out with five replicates. The morphology of INDs was determined with high-resolution Transmission Electron Microscopy (TEM) (FEI Tecnai F20 XT Field Emission TEM) using a lacey carbon coated copper grid (TED PELLA, Redding, CA).

Optical absorption spectra of INDs suspended in DI water (1 mg/mL) were measured at room temperature by using a UV-Vis spectrophotometer (U-3310, Hitachi) in a glass cuvette with an optical path of 10 mm. Un-irradiated NDs were used as the reference. The optical characterization of the INDs was performed using the same PA setup as described in our previous study [42]. A DI water suspension of INDs was injected into Tygon tubing (1 mm ID, 1.78 mm OD), which was immersed in water. The PA amplitude of INDs at different wavelengths was recorded with five replicates.

2.3 Cell Culture and *In Vitro* Cytotoxicity

Murine mammary tumor 4T1.2 is known for its highly metastatic pattern, which mimics closely to that of human breast cancer. 4T1.2-neu was established by the transformation of 4T1.2 to express oncogene HER2/Neu [43]. The 4T1.2 and 4T1.2-neu breast cancer cells were cultured in DMEM containing 10% FBS and 1% L-glutamine at 37 °C supplied with 5% CO_2 under a humidified environment. The 4T1.2-neu cells (5000/well) were seeded onto 96-well plates in 100 μL of culture media and incubated for 24 hr. HER2-PEG-INDs in 10 μL of PBS were added at a series of final concentrations (10, 50, 100, 150 and 200 μg/mL). After incubation for 48 h, the cell viability was evaluated by the Resazurin-blue assay.

2.4 Cellular Uptake and Imaging

To quantify the cellular uptake of INDs and image nanoparticles inside the cells, INDs, PEG-INDs and HER-PEG-INDs were labeled with a fluorescent dye. Briefly, 500 μg of PEG-INDs or HER2-PEG-INDs were dissolved in 500 μL of sodium borate buffer (10 mM, pH 8.5), followed by the addition of Cyanine7 (Cy7) NHS ester (100 μg in 10 μL of DMSO). The mixture was stirred overnight at room temperature in the dark and the resulting nanoparticles were separated from the solution by centrifuge, washed with DI water/ethanol (v/v, 1:1) three times and dried in a SpeedVap concentrator (Labconco Corp.). To determine the cellular uptake of PEG-INDs and HER2-PEG-INDs, cells were seeded onto 12-well plates at a density of 25×10^4 and incubated for 24 hr. 4T1.2-neu cells were treated with Cy7-PEG-INDs or Cy7-HER2-PEG-INDs at a final concentration of 5 μg/mL (based on INDs), whereas 4T1.2 cells were treated with Cy7-HER2-PEG-INDs at a final concentration of 5 μg/mL (based on INDs) followed by incubation at 37 °C for 6 hr. Then the cells were washed three times with 3 mL of PBS and removed after incubation with 50 μL lysis buffer [5 mmol/L EDTA, 10 mmol/L NaOH, 10 mmol/L Tris base, 150 mmol/L NaCl and 1% (v/v) Triton X-100] for 10 min at room temperature. Another 450 μL of DI water was added to each well, and the fluorescence intensity of the resulting cell lysate samples were analyzed based on a standard curve of free Cy7 NHS ester solution prepared in 1:3 (v/v) lysis buffer/DI water. The cell protein content was quantified using a Pierce™ BCA protein assay (Thermo Scientific). For the HER2 competitive inhibition experiments, cells were exposed to anti-HER2 peptide (0.75 μg/mL) for 1 h before the incubation with Cy7-PEG-INDs or Cy7-HER2-PEG-INDs (10 μg/mL based on INDs) for 3 hr. The cell lysis procedures and analysis methods were identical to the cellular uptake study.

Cells were seeded onto poly-L-lysine precoated glass coverslips (BD, Franklin Lakes, NJ) in 12-well culture plates at a density of 50,000 cells per well and grown overnight. 4T1.2-neu cells were treated with or without 32 μg of PEG-INDs or HER2-PEG-INDs (based on INDs), whereas 4T1.2 cells were treated with or without 32 μg of HER2-PEG-INDs (based on INDs) followed by incubation at 37 °C for 4 hr. Then the cells were washed three times with 3 mL of PBS and imaged using an inverted microscope (Eclipse TE2000-U, Nikon).

2.4 Photoacoustic Imaging

The experimental setup for PA imaging of biological tissues has been described before [42, 44]. The deep reflection-mode PA imaging system is capable of sub 0.2-mm resolution at depths of 19 mm and penetration of up to 38 mm [45]. A 532-nm Q-switched Nd:YAG laser (Surelite III, Continuum) pumped an optical parametric oscillator laser (Surelite OPO PLUS, Continuum) with 6-ns pulses at a repetition rate of 10 Hz, and an optical condenser transformed the laser output to a ring-shape illumination, which was confocal with the ultrasonic transducer in the targeted area. The illumination beam had a diameter of 7 mm on the tissue surface, and the laser fluence was 18 mJ/cm^2, which was lower than laser safety limits (20 mJ/cm^2) recommended by the American National Standards Institute (ANSI). A 5-MHz transducer (35-mm focal length; 70% −6-dB fractional bandwidth, SU-108-013, Sonic Concepts) collected the photoacoustic signals, which were amplified by a pre-amplifier (5072PR, Olympus-NDT) and then collected by a PC through an A/D scope card

(CS21G8-256MS, Gage) with 8-bit resolution and a 125-MHz sampling rate for forming and analyzing PA images using MATLAB® software (Mathworks, Natick, MA).

Animal studies used female BALB/c mice in accordance with an approved protocol under the guidance of the Institutional Animal Care and Use Committee at the University of Kansas. The murine breast cancer cells, 4T1.2 and 4T1.2-neu, were prepared in PBS at a concentration of 2×10^7 cells/mL, and were kept in an ice bath before injection. Mice were anesthetized with 1.5% isoflurane in 1:1 oxygen-air mixture, and a 50-μL cell suspension was injected subcutaneously into the right mammary fat pad under the second nipple and along the lateral line of the mice using a 30-ga needle. Mice were ready for PA imaging when the breast cancer tumors obtained dimensions of *ca.* 5 × 5 mm, as measured with a digital caliper.

Before each imaging experiment, the animals were anesthetized with a mixture of ketamine (87 mg/kg body weight) and xylazine (13 mg/kg body weight). The right breast areas of mice were depilated using surgical hair removal lotion to avoid the interference from hairs to ultrasound propagation. The mice were maintained under anesthesia on a warm pad and underneath the membrane in the center of the bottom of the water tank during the entire imaging process. Between the skin and the membrane, ultrasound gel was applied as a coupling medium. The breathing rate of mice was visually monitored and maintained at one breath per two seconds. PA images of the breast tumor areas were obtained as background images before injecting PEG-INDs or HER2-PEG-INDs particles. After determining the depth of the detector's focal point (2 – 3 mm) along with the imaging resolution of *ca.* 270 μm, particles were administrated intravenously via the tail vein. The tumor areas were scanned continuously and repeatedly at a rate of 20 min per scan at a laser wavelength of 820 nm.

The signal intensity of the tumor area was measured using ImageJ software (v 1.46r, http://imagej.nih.gov/ij/). PA images were converted to grayscale images, followed by the quantification of PA signal intensity of the tumor region by measuring the mean gray values (unit: gray/pixel). The extent of signal enhancement was calculated with the following equation: increase in PA signal = [(intensity of each time point - intensity of background image)/intensity of background image)] × 100%.

2.5 Hemolysis and Platelet Coagualtion Assay

Fresh rat whole blood from a female Sprague-Dawley rat was stabilized with EDTA. Serum was removed from the blood sample by centrifugation at 1200 × g for 5 min at room temperature, and the remaining red blood cells (RBCs) were washed 5 times with isotonic PBS and then diluted 10 times with the same solution after the last wash. Diluted RBCs suspension (0.02 mL, *ca.* 4×10^8 cells/mL) was added to the nanoparticle suspension (0.08 mL) prepared with PBS at a concentration of 100 μg/mL. After vortexing, the mixtures were incubated at room temperature for 2 h, and then samples were centrifuged for 5 min at 1500 × g to remove nanoparticles and intact RBCs. The absorbance of the hemoglobin in the supernatant at 570 nm was measured. Triton X-100 (1%) and PBS were used as positive and negative controls, respectively.

Platelet aggregation was assessed by tracking changes in the particle size using a Coulter particle counter (Coulter Multisizer 4, Beckman Coulter, Pasadena, CA). Fresh rat whole blood was withdrawn and placed in heparinized tubes (BD Vacutainer® Lithium Heparin 37 USP unit, BD Franklin Lakes, NJ). Blood was centrifuged at 150 × g for 15 min to obtain platelet-rich plasma (PRP). PRP was pretreated with ADP sodium salt (0.5 μM), PBS, or INDs (20, 50 and 100 μg/mL). The mixtures were incubated at 37 °C for 3 min. After dilution in Isoton II electrolyte (Coulter Electronics), particle sizes of platelet aggregates were measured using a 50-μm aperture tube.

2.6 Histopathological Examination

Animals were euthanized 12 hr after injection of INDs or saline, and the kidneys and livers were resected and fixed in 10% formalin. A blinded board-certified pathologist at Lawrence Memorial Hospital (Lawrence, KS) conducted pathological examinations; sections and recut sections of kidneys and livers in both groups were stained with hematoxylin and eosin (H & E) and microscopically examined.

2.6 Statistical Analysis

GraphPad Prism 5 software was used for statistical analysis. The difference between two data sets were analyzed using *t*-test, while a one-way ANOVA was used for analyzing the differences among experimental and control groups. In all comparisons, a p value of ≤ 0.05 [marked with an asterisk (*) in figures] was considered to be statistically significant.

3. Results

3.1. Synthesis and Characterization

The TEM image of the bare INDs after radiation and acid treatment is presented in Figure 1. INDs exhibited quadrilateral shapes with an average diameter of *ca.* 38 nm.

For INDs irradiated by 40-keV He^+ ions at a dose of ca. 3×10^{15} He^+/cm^2, our previous experiments have estimated that they contain an ensemble of vacancies with a density in the range of ca. 3000 ppm [39]. Creating vacancies in such a high density often results in amorphization of diamond as well as severe broadening of the optical absorption bands [46, 47]. No distinct zero-phonon line corresponding to GR1, i.e. the isolated neutral vacancy center, could be detected at 741 nm [48]. Instead, the UV-Vis spectrum of the INDs shows a monotonic increase in absorbance from 850 to 450 nm (Figure 2), similar to those of carbon black and other carbon nanomaterials [49]. PA signal amplitude showed a similar decreasing trend from 680 nm to 900 nm.

Since photoacoustic imaging is an absorption-based technology, the PA signal amplitude decreased in proportion to the decline of the optical absorption in the tunable wavelength range of the PA imaging system. Although the small bump at 720 nm in the PA spectrum is not shown in the UV-Vis absorption spectrum, the signal intensity dropped 50% from 700 nm to 840 nm, which was the same trend as the absorption spectrum. The tumor areas of mice bearing breast cancer were imaged at 820 nm. Although INDs had stronger absorption and thus higher contrast against background tissues at 700 nm comparing to 820 nm, the

signal contributions from blood vessel would also be greater [50]. An imaging wavelength of 820 nm was chosen for *in vivo* studies because the absorption of hemoglobin and Mie scattering is minimized, and the PA signal enhancement is more pronounced in the images due to the accumulation of IND particles.

Conjugation of amine-PEG-amine (MW 2000) and anti-HER2 targeting peptide to the INDs was verified by FTIR (Figure 3). The appearance of the characteristic peaks of the PEG, at 1250 and 1035 cm^{-1}, confirmed the presence of the coating on the surface of bare INDs. In addition, the FTIR spectrum of HER2-PEG-INDs displayed the same intense peaks as anti-HER2 peptide at 1656 and 1521 cm^{-1}, corresponding to the stretching vibration of the amino group on lysine and hydroxyl group on tyrosine, respectively. The band at 1200–1260 cm^{-1} resulted from the -OH stretching vibration in the serine.

In addition to the FTIR spectra, the coating of PEG and HER2 targeting peptide was further confirmed by the hydrodynamic diameters and zeta potentials of the INDs and the surface-functionalized INDs. Table 1 shows the progressive increase in particle size and decrease in negative charge of the nanoparticle surfaces. The decrease in the negative charges was due to the introduction of amino groups from amine-PEG-amino and lysine residues in the anti-HER2 peptides.

Both FTIR spectra and increased particle sizes are consistent with the introduction of HER2 targeting peptide onto the INDs via the linkage to amine-PEG-amine. We assumed *ca.* 10% of the carboxyl groups on the INDs were reacted with amine-PEG-amine, which was described similarly before, and that amino group on INDs were conjugated with anti-HER2 peptide in a 1:1:1 ratio. Consequently, yield for the amount of targeting peptide on the surface of INDs was expected to be *ca.* 10^{-5} mol/g[51]. Using UV-absorbance, the labeling was determined to be *ca.* 8.6×10^{-5} moles of HER2 targeting peptide per gram of PEG-IND nanoparticles (see Supporting Information).

3.2 Cytotoxicity, Cellular Uptake and Cellular Imaging

In order to evaluate the cytotoxicity of HER2-PEG-INDs and the potential for biological applications, 4T1.2-neu cells were incubated with particles for 48 h at concentrations ranging from 10 to 200 μg/mL. As shown in Figure 4, there was a dose-dependent decrease in cell viability above 10 μg/mL, and the cells retained viability up to 90% at concentrations of 10 and 50 μg/mL after 48 h. However, a reduction in cell viability was observed at higher concentrations.

The targeting ability of anti-HER2-peptide to HER-overexpressing breast cancer cells was evaluated by measuring the intracellular fluorescence intensity after treatment of HER2-positive and –negative cells with Cy7-labeled INDs. In Figure 5a, significantly increased cellular accumulation of HER2-PEG-INDs by 4T1.2-neu cells was observed. This result can be explained by that HER2-PEG-INDs was taken up via HER2 receptor mediated endocytosis. Thus, a competitive inhition assay was performed to confirm the target-specific uptake behavior of anti-HER2 peptide conjugated INDs. Not surprisingly, remarkly suppressed internalization of HER-PEG-INDs by 4T1.2-neu cells was found as anti-HER2 peptide (0.75 μg/mL) was added to the media 1 hr before the addition of INDs (Figure 5b).

This result suggested that the uptake of HER2-PEG-INDs was hindered effectively by reducing the availability of HER2 receptors on the surface of 4T1.2-neu tumor cells. In contrast, the internalization of PEG-INDs by 4T1.2-neu cells and HER2-PEG-INDs by 4T1.2 cells remained unaffected in the presence of anti-HER2 peptide.

The cellular uptake anti-HER2 peptide was confirmed *in vitro* by the brightfield images of INDs interactions with HER2 receptor positive and negative breast cancer cells (4T1.2-neu and 4T1.2 cells) (Figure 6). As negative controls, 4T1.2-neu breast cancer cells were treated with non-targeted PEGylated INDs (4T1.2-neu cells + PEG-INDs) and HER2 negative 4T1.2 cells were treated with targeted PEGylated INDs (4T1.2 cells + HER2-PEG-INDs). The clusters of IND particles present black spots in the cells. There was no obvious accumulation of INDs in the control groups after 4 hr of incubation (Figure 6b and 6d). By contrast, HER2-PEG-INDs, which contain the HER2 targeting peptide, accumulated to a greater degree inside cells and on the cell membranes (Figure 6e). This indicated that the HER2-specific peptide increased the cellular uptake of HER2-PEG-INDs by HER2 over-expressing cells. This result was further confirmed by comparing the fluorescence images of breast cancer cells incubated with Cy7 labeled INDs (Supporting Informations Figure S2). The amount of HER2-PEG-INDs internalized by HER2-overexpressing cells was apparently larger than that of INDs internalized by cells without targeting effect.

3.3 In Vivo PA Imaging

Prior to the injection, a region of interest (ROI) was selected on the right side of the breast and defined as background (BG). The depth of the detector's focal point was adjusted so as to obtain the best spatial resolution. BALB/C mice were injected with identical amounts of INDs via the tail vein. Once the depth of the detector's focal point was determined, PA images of the same areas were taken with 1-hr intervals and processed to remove the skin's signal as illustrated in Figure 7. The three control groups were the HER2 positive tumor model (4T1.2-neu) treated with saline (Figure 7a), HER2 positive tumor model (4T1.2-neu) treated with PEG-INDs (Figure 7b) and the HER2 negative tumor model (4T1.2) treated with HER2-PEG-INDs (Figure 7c). In the PA images, the blood vessels (BVs) were highlighted because of the relatively higher optical absorption of hemoglobin over normal optically transparent tissues. Signal intensity did not significantly increase in the saline group until 8 hrs post-injection (Figure 7a). Beginning at 2 hrs post-injection, the blood contrast was enhanced as indicated by the colorbars in the figures, and signal intensity peaked at 4 to 6 hrs in each group. Meanwhile, IND particles progressively migrated from the blood vessels into internal tumor regions, presumably due to the enhanced permeability and retention (EPR) effect and retention by the HER2-positive cancer cells. The HER2-positive breast cancer model treated with HER2-PEG-INDs had higher signal enhancement around the tumor region that finally delineated the entire tumor (dashed circle in Figure 7d) at 8 hrs, compared to the HER2-negative tumors and untargeted INDs in the HER2 positive tumors (Figure 7e).

The hemolytic activity of INDs was conducted by a colorimetic assay of the iron-containing protein hemoglobin released by damaged cells upon exposure to INDs. As shown in Figure 8a, all INDs did not induce RBC destruction at the concentration as high as 100 μg/mL. In

order to further investigate the hematocompatibility of INDs, platelet aggregation behavior was performed by incubating INDs with PRP at 37 °C for 3 min and measuring the averaged particle sizes of platelet aggregates. Compared to the positive and negative controls (Figure 8b), the average particle size did not significantly change at the highest concentrations tested (100 μg/mL). In addition, no platelet aggragation was induced by INDs at lower concentrations (data not shown). Furthermore, the hematology biocompatibility of INDs with mice was assessed by measuring the hematological parameters, including leukocytes, lymphocytes, erythrocytes and mean hemoglubin, and biomakers of liver damage, aspartate aminotransferase (AST) and alanine aminotransferase (ALT). The results in Table S1 showed that there were no significant changes in these parameter values and thus no significant inflammation induced after exposure to HER2-PEG-INDs, compared to saline.

3.4 Histopathological Examination

No significant histopathological abnormalities were observed in the kidneys nor livers of mice injected with INDs compared to saline injected mice, and no inflammation was observed by H&E staining (Figure 9 and Figure S3), which demonstrated no apparent toxicity of these INDs to the renal and hepatic organs at 12 hr after *i.v.* administration.

4. Discussion

The HER2 receptor is overexpressed in 25% to 30% breast cancers and has been exploited as a molecular target for delivery of drugs and nanoparticles for biomedical applications [52, 53]. The HER2-targeting peptide (KCCYSL) is relatively small, but it exhibited high affinity (295 ± 56 nmol/L) to the HER2 receptor [37]. Due to its small size, this anti-HER2 peptide can be conjugated to the surface of nanoparticles with higher density in comparison to larger HER2-targeting antibodies. As a result, cellular uptake was enhanced leading to rapid entrance of nanoparticles into the tumor cells. In addition, the peptide-targeting moiety may have less immunogenicity and cytotoxicity than antibody-based ones because of its lower molecular weight [54]. Uptake of the peptide-nanoparticle conjugate in 4T1.2-neu breast cancer cells was appreciably higher than that of PEGylated INDs (Figure 5a). Meanwhile, owing to the specific binding of HER2-PEG-INDs to the tumor, the nanoparticle clearance rate from blood circulation was decreased and the loss of nanoparticles was minimized (Figure S2) [55]. For this reason, limited accumulation and rapid clearance of non-targeted INDs in the control groups made it difficult to differentiate the tumor regions in PA images. Whereas, the tumors in mice treated with HER-PEG-INDs were fully delineated by strong contrast between the tumor regions and surrounding tissues. This result is further confirmed by the prolonged retention time within tumors in the HER2 targeted treatment group. The prolonged presence of contrast agent in the tumor is critical for PA assisted cancer detection. So, the signal intensity of the tumor region was monitored and compared between two consecutive scans until a decrease in signal amplitude was observed. The maximum accumulation of HER2-PEG-INDs in HER-overexpressing tumor bearing mice was at 8 hrs post-injection, contrasted with 6 hrs in the control groups (Figure 10, $p < 0.05$, $n = 3$). Furthermore, the HER2-PEG-INDs had a more rapid uptake and a relatively slower clearance rate in the HER2-positive tumor model. The PA signal was significantly enhanced in the HER2-positive tumor region after 2 hrs (Figure 7e), and there

was no evidence of a signal decrease until 11 hrs post-injection (Figure 7d). However, in the HER2-negative and non-targeted control groups, PA amplitude increased slowly and then declined rapidly within one hour (Figure 7b and 7c). Since the rate of extravasation from the poorly formed blood vessels into the tumor region and the rate of clearance are two major factors that affect the nanoparticle accumulation in the tumor, strong binding between the HER2-targeting peptide and HER2 receptor on the cell surface may favor the retention of HER2-PEG-INDs. Thus, even though PEG-INDs and HER2-PEG-INDs may have a similar opportunity to leak from the blood vessels due to the EPR effect, the differences in such factors as retention and cellular uptake resulted in quite different tumor accumulations of INDs and thus the accumulative PA signal enhancement.

Owing to the EPR effect, nano-sized particles or macromolecules administrated intravenously escape renal clearance and tend to leak out from the abnormal vasculature and accumulate in solid tumors [56]. However, Li M.L. *etc* demonstrated that gold nanoshells could not actually enter the necrotic tissues of tumor but accumulated within the tumor cortex, and the nanoshells delineated the tumor margins when imaged by PA microscopy at a wavelength of 800 nm [57]. The absence of INDs within the tumor core can be explained by both the necrotic feature and high interstitial pressure of tumor cores [58]. In addition, the observation of no INDs on the top surface of the tumor may be explained by the pressure from the water tank above the tumor area, which may hinder the circulation and particle accumulation.

Among carbon-based nanomaterials, NDs are considered to be less toxic than carbon nanotubes and graphene oxide [59]. This is mainly because of diamond's unique properties of sp^3 electron configuration, chemical inertness and especially due to the purification process in strong acid used to remove impurities and graphitic surface layers [24]. It has been demonstrated that carboxylated NDs internalized by macropinocytosis and endocytosis pathways did not show noticeable cytotoxicity or affect cell proliferation and differentiation [60], which was also indicated by our cytotoxicity study (Figure 4). *In vivo* biodistribution of NDs has been studied by positron emission tomography after labeling nanoparticles with ^{18}F. The lungs, spleen and liver were the primary accumulating locations of NDs, and particles were excreted in urine beginning at 2 hr after *i.v.* administration [61]. On the basis of this study, we collected the kidneys, lung and liver 12 hr after injection of HER2-PEG-INDs for histopathological examination, and we did not observe any indications of toxicity (Figure S3). This is consistent with other reports of the *in vivo* biocompatibility of NDs after multiple routes of administration [62, 63]. In addition, the long-term biocompatibility of INDs 12 weeks after intraperitoneal injection has been demonstrated by our group in a prior report [26]. Although the toxicity of these HER2-PEG-INDs needs to be systematically investigated and analyzed comprehensively before application in the clinic, our results have shown the biocompatibility and potential utility of HER2-targeting INDs for biomedical applications.

5. Conclusions

In this work, non-toxic, stable and targeted non-fluorescent INDs were successfully developed as a novel *in vivo* PA imaging contrast agent and shown to facilitate the optical

contrast enhancement of breast tumor margins. The conjugation of PEGylated INDs with anti-HER2 peptide lead to an enhancement in the internalization by HER2 overexpressing tumor cells (4T1.2-neu) and longer residence time in the region of HER2 positive tumor. We expect this targeted IND-PA imaging platform to provide a new oppotunity for sensitive phenotype specific detection of tumors.

6. Futher perspective

With the outstanding advantages of high optical absorption, photostability and biocompatibility, targeted IND conjugates can be used as a molecularly selective contrast agent for photoacoustic detection of cancers. The HER2 targeting peptide significantly improved the efficiency and specificity of delivery of INDs to HER2-positive breast tumors. It is expected that HER2-targed INDs may offer an effective means for early detection of HER2-positive breast cancers.

7. Executive summary

Preparation of human epidermal growth factor receptor-2 (HER2)-PEG-irradiated nanodiamonds (INDs)

- The HER2-PEG-INDs were designed to serve as a molecularly-targeted photoacoustic (PA) contrast agent for detection of HER2-positive breast cancer.

Cellular uptake of HER2-PEG-INDs by the HER2-positive tumor cells

- When conjugated with HER2-specific peptide, the internalization of INDs by HER-positive cells was significantly increased compared to control groups.

Photoacoustic imaging of breast tumor

- The entire breast tumor area was completely delineated by the enhanced PA signal due to the accumulation of HER2-PEG-INDs in the HER-positive tumor model after *i.v.* injection.

Histopathological examination for toxicity

- 12 hr after *i.v.* administration of INDs, no apparent histopathological abnormalities nor inflammation were observed in the kidneys or livers of mice.

Conclusion

- The author’s study has demonstrated the first use of non-toxic INDs for phenotype detection and delineation of tumors.
- The HER2-targeting peptide resulted in improved tumor uptake and longer residence time of INDs in the tumor region, and thus enhanced the PA imaging contrast.
- This targeted-nanodiamond-PA imaging platform has potential as a more effective alternative to biopsy and nuclear imaging for sensitive detection of cancers.

Acknowledgments

This work was funded in part by the National Institutes of Health (1R01CA173292-01, PI MLF) and American Cancer Society (RSG-0813301CDD, PI MLF). We thank Dr. Detamore and Vineet Gupta for the use of their Coulter Multisizer.

References

* of interest

** of considerable interest

1. Ravnan MC, Ravnan SL, Walberg MP. Metastatic breast cancer: A review of current and novel pharmacotherapy. Formulary. 2011; 46(4):130.
2. Vogel CL, Cobleigh MA, Tripathy D, et al. Efficacy and safety of trastuzumab as a single agent in first-line treatment of HER2-overexpressing metastatic breast cancer. J Clin Oncol. 2002; 20(3): 719–726. [PubMed: 11821453]
3*. Mallidi S, Luke GP, Emelianov S. Photoacoustic imaging in cancer detection, diagnosis, and treatment guidance. Trends Biotechnol. 2011; 29(5):213–221. A comprehensive review regarding the applications of the photoacoustic imaging in cancer detection. [PubMed: 21324541]
4. Yao JJ, Wang LHV. Photoacoustic tomography: fundamentals, advances and prospects. Contrast Media Mol Imaging. 2011; 6(5):332–345. [PubMed: 22025335]
5. De La Zerda A, Kim JW, Galanzha EI, Gambhir SS, Zharov VP. Advanced contrast nanoagents for photoacoustic molecular imaging, cytometry, blood test and photothermal theranostics. Contrast Media Mol Imaging. 2011; 6(5):346–369. [PubMed: 22025336]
6. Ntziachristos V, Bremer C, Weissleder R. Fluorescence imaging with near-infrared light: new technological advances that enable in vivo molecular imaging. Eur Radiol. 2003; 13(1):195–208. [PubMed: 12541130]
7. Filonov GS, Krumholz A, Xia J, Yao JJ, Wang LHV, Verkhusha VV. Deep-Tissue Photoacoustic Tomography of a Genetically Encoded Near-Infrared Fluorescent Probe. Angew Chem Int Ed Engl. 2012; 51(6):1448–1451. [PubMed: 22213541]
8. Zhang HF, Maslov K, Stoica G, Wang LHV. Functional photoacoustic microscopy for high-resolution and noninvasive in vivo imaging. Nat Biotechnol. 2006; 24(7):848–851. [PubMed: 16823374]
9. Wang LHV. Ultrasound-mediated biophotonic imaging: A review of acousto-optical tomography and photo-acoustic tomography. Dis Markers. 2003; 19(2–3):123–138. [PubMed: 15096709]
10. Hahn MA, Singh AK, Sharma P, Brown SC, Moudgil BM. Nanoparticles as contrast agents for in-vivo bioimaging: current status and future perspectives. Anal Bioanal Chem. 2011; 399(1):3–27. [PubMed: 20924568]
11. Kolkman RGM, Hondebrink E, Steenbergen W, Van Leeuwen TG, De Mul FFM. Photoacoustic imaging of blood vessels with a double-ring sensor featuring a narrow angular aperture. J Biomed Opt. 2004; 9(6):1327–1335. [PubMed: 15568955]
12. Siphanto RI, Thumma KK, Kolkman RGM, et al. Serial noninvasive photoacoustic imaging of neovascularization in tumor angiogenesis. Opt Express. 2005; 13(1):89–95. [PubMed: 19488331]
13. Wang XD, Xie XY, Ku GN, Wang LHV. Noninvasive imaging of hemoglobin concentration and oxygenation in the rat brain using high-resolution photoacoustic tomography. J Biomed Opt. 2006; 11(2)
14. Shashkov EV, Everts M, Galanzha EI, Zharov VP. Quantum Dots as Multimodal Photoacoustic and Photothermal Contrast Agents. Nano Lett. 2008; 8(11):3953–3958. [PubMed: 18834183]
15. Tam JM, Tam JO, Murthy A, et al. Controlled Assembly of Biodegradable Plasmonic Nanoclusters for Near-Infrared Imaging and Therapeutic Applications. ACS Nano. 2010; 4(4):2178–2184. [PubMed: 20373747]
16. Kim C, Qin RG, Xu JS, Wang LV, Xu R. Multifunctional microbubbles and nanobubbles for photoacoustic and ultrasound imaging. J Biomed Opt. 2010; 15(1)

17. Cheng K, Cheng Z. Near Infrared Receptor-Targeted Nanoprobes for Early Diagnosis of Cancers. Curr Med Chem. 2012; 19(28):4767–4785. [PubMed: 22873665]

18. Kim C, Favazza C, Wang LHV. In Vivo Photoacoustic Tomography of Chemicals: High-Resolution Functional and Molecular Optical Imaging at New Depths. Chem Rev. 2010; 110(5): 2756–2782. [PubMed: 20210338]

19. Nguyen Ngoc Long LVV, Kiem Chu Dinh, Doanh Sai Cong, Nguyet Cao Thi, Hang Pham Thi, Thien Nguyen Duy, Quynh Luu Manh. Synthesis and optical properties of colloidal gold nanoparticles. J Phys Conf Ser. 2009; 187:9.

20. Huang P, Bao L, Zhang CL, et al. Folic acid-conjugated Silica-modified gold nanorods for X-ray/CT imaging-guided dual-mode radiation and photo-thermal therapy. Biomaterials. 2011; 32(36):9796–9809. [PubMed: 21917309]

21*. Wijaya A, Schaffer SB, Pallares IG, Hamad-Schifferli K. Selective Release of Multiple DNA Oligonucleotides from Gold Nanorods. ACS Nano. 2009; 3(1):80–86. A report of thermally induced deformation of gold nanorods under near-infrared light for the selective release of DNA Oligonucleotides. [PubMed: 19206252]

22. Chen CC, Lin YP, Wang CW, et al. DNA-gold nanorod conjugates for remote control of localized gene expression by near infrared irradiation. J Am Chem Soc. 2006; 128(11):3709–3715. [PubMed: 16536544]

23. Yah CS. The toxicity of Gold Nanoparticles in relation to their physiochemical properties. Biomedical Research-India. 2013; 24(3):400–413.

24. Mochalin VN, Shenderova O, Ho D, Gogotsi Y. The properties and applications of nanodiamonds. Nat Nanotechnol. 2012; 7(1):11–23. [PubMed: 22179567]

25**. Chang YR, Lee HY, Chen K, et al. Mass production and dynamic imaging of fluorescent nanodiamonds. Nat Nanotechnol. 2008; 3(5):284–288. Reports a new nanomaterial, fluorescent nanodiamonds, can be produced in large quantities by the irradiation and is suitable for biological imaging applications. [PubMed: 18654525]

26**. Vaijayanthimala V, Cheng PY, Yeh SH, et al. The long-term stability and biocompatibility of fluorescent nanodiamond as an in vivo contrast agent. Biomaterials. 2012; 33(31):7794–7802. Reports the acceptable bio-stability and long-term biocompatibility of fluorescent nanodiamonds for *in vivo* applications. [PubMed: 22863379]

27. Vaijayanthimala V, Tzeng YK, Chang HC, Li CL. The biocompatibility of fluorescent nanodiamonds and their mechanism of cellular uptake. Nanotechnology. 2009; 20(42)

28. Hegyi A, Yablonovitch E. Molecular Imaging by Optically Detected Electron Spin Resonance of Nitrogen-Vacancies in Nanodiamonds. Nano Lett. 2013; 13(3):1173–1178. [PubMed: 23384363]

29. Zhang XY, Wang SQ, Zhu CY, et al. Carbon-dots derived from nanodiamond: Photoluminescence tunable nanoparticles for cell imaging. J Colloid Interface Sci. 2013; 397:39–44. [PubMed: 23484769]

30. Nakamura T, Ohana T, Yabuno H, Kasai R, Suzuki T, Hasebe T. Simple Fabrication of Gd(III)-DTPA-Nanodiamond Particles by Chemical Modification for Use as Magnetic Resonance Imaging (MRI) Contrast Agent. Appl Phys Express. 2013; 6(1)

31. Baum RP, Prasad V, Muller D, et al. Molecular Imaging of HER2-Expressing Malignant Tumors in Breast Cancer Patients Using Synthetic In-111- or Ga-68-Labeled Affibody Molecules. J Nucl Med. 2010; 51(6):892–897. [PubMed: 20484419]

32. Loo C, Lowery A, Halas NJ, West J, Drezek R. Immunotargeted nanoshells for integrated cancer imaging and therapy. Nano Lett. 2005; 5(4):709–711. [PubMed: 15826113]

33. Romond EH, Perez EA, Bryant J, et al. Trastuzumab plus adjuvant chemotherapy for operable HER2-positive breast cancer. N Engl J Med. 2005; 353(16):1673–1684. [PubMed: 16236738]

34. slamon DJ, Leyland-Jones B, Shak S, et al. Angewandte Chemie. International Edition in Englishangewandte Chemie International Edition in Englishangewandte Chemie-International Edition. Use of chemotherapy plus a monoclonal antibody against HER2 for metastatic breast cancer that overexpresses HER2. N Engl J Med. 2001; 344(11):783–792. [PubMed: 11248153]

35*. Tai WY, Mahato R, Cheng K. The role of HER2 in cancer therapy and targeted drug delivery. J Control Release. 2010; 146(3):264–275. A recent review concerning the importance of HER2 in cancer therapy and targeted drug delivery. [PubMed: 20385184]

36*. Tai WY, Shukla RS, Qin B, Li BY, Cheng K. Development of a Peptide-Drug Conjugate for Prostate Cancer Therapy. Mol Pharm. 2011; 8(3):901–912. Development and application of HER2 targeting peptide drug conjugates for prostate cancer therapy. [PubMed: 21510670]

37. Kumar SR, Quinn TP, Deutscher SL. Evaluation of an In-111-Radiolabeled peptide as a targeting and Imaging agent for ErbB-2 receptor-expressing breast carcinomas. Clin Cancer Res. 2007; 13(20):6070–6079. [PubMed: 17947470]

38. Su LJ, Fang CY, Chang YT, et al. Creation of high density ensembles of nitrogen-vacancy centers in nitrogen-rich type Ib nanodiamonds. Nanotechnology. 2013; 24(31):315702. [PubMed: 23857995]

39. Wee T-L, Mau Y-W, Fang C-Y, Hsu H-L, Han C-C, Chang H-C. Preparation and characterization of green fluorescent nanodiamonds for biological applications. Diam Relat Mater. 2009; 18(2–3): 567–573.

40*. Dahoumane SA, Nguyen MN, Thorel A, Boudou JP, Chehimi MM, Mangeney C. Protein-Functionalized Hairy Diamond Nanoparticles. Langmuir. 2009; 25(17):9633–9638. Reports a new application of nanodiamonds as an optical contrast agent for photoacoustic imaging, and demonstrates their capability of deep imaging. [PubMed: 19634873]

41. Lim TS, Fu CC, Lee KC, et al. Fluorescence enhancement and lifetime modification of single nanodiamonds near a nanocrystalline silver surface. Phys Chem Chem Phys. 2009; 11(10):1508–1514. [PubMed: 19240927]

42. Zhang T, Cui HZ, Fang CY, et al. Photoacoustic contrast imaging of biological tissues with nanodiamonds fabricated for high near-infrared absorbance. J Biomed Opt. 2013; 18(2)

43. Kim JH, Majumder N, Lin H, Chen J, Falo LD Jr. You Z Enhanced immunity by NeuEDhsp70 DNA vaccine Is needed to combat an aggressive spontaneous metastatic breast cancer. Mol Ther. 2005; 11(6):941–949. [PubMed: 15922965]

44. Cui HZ, Yang XM. In vivo imaging and treatment of solid tumor using integrated photoacoustic imaging and high intensity focused ultrasound system. Med Phys. 2010; 37(9):4777–4781. [PubMed: 20964197]

45. Song KH, Wang LV. Deep reflection-mode photoacoustic imaging of biological tissue. J Biomed Opt. 2007; 12(6):060503. [PubMed: 18163798]

46. Brunetto R, Baratta GA, Strazzulla G. Amorphization of diamond by ion irradiation: a Raman study. J Phys Conf Ser. 2005; 6:120–125.

47. Khomich AV, Khmelnitskiy RA, Dravin VA, Gippius AA, Zavedeev EV, Vlasov. Radiation damage in diamonds subjected to helium implantation. Phys Solid State. 2007; 49(9):1661–1665.

48. Davies G, Lawson SC, Collins AT, Mainwood A, Sharp SJ. VACANCY-RELATED CENTERS IN DIAMOND. Physical Review B. 1992; 46(20):13157–13170.

49. Zhao B, Itkis ME, Niyogi S, Hu H, Zhang J, Haddon RC. Study of the extinction coefficients of single-walled carbon nanotubes and related carbon materials. J Phys Chem B. 2004; 108(24): 8136–8141.

50. Castano AP, Demidova TN, Hamblin MR. Mechanisms in photodynamic therapy: part one-photosensitizers, photochemistry and cellular localization. Photodiagnosis Photodyn Ther. 2004; 1(4):279–293. [PubMed: 25048432]

51. Zhang BL, Li YQ, Fang CY, et al. Receptor-Mediated Cellular Uptake of Folate-Conjugated Fluorescent Nanodiamonds: A Combined Ensemble and Single-Particle Study. Small. 2009; 5(23): 2716–2721. [PubMed: 19743434]

52**. Raju A, Muthu MS, Feng S-S. Trastuzumab-conjugated vitamin E TPGS liposomes for sustained and targeted delivery of docetaxel. Expert Opin Drug Deliv. 2013; 10(6):747–760. Cytotoxicity of three kinds of carbon nanomaterials was examined and compared. Among the carbon nanomaterials, nanodiamonds exhibited the least cytotoxicity along with the highest cellular uptake. [PubMed: 23458409]

53. Wang Y, Liu P, Du J, Sun Y, Li F, Duan Y. Targeted siRNA delivery by anti-HER2 antibody-modified nanoparticles of mPEG-chitosan diblock copolymer. J Biomater Sci Polym Ed. 2013; 24(10):1219–1232. [PubMed: 23713424]

54. Kawamoto M, Horibe T, Kohno M, Kawakami K. HER2-Targeted Hybrid Peptide That Blocks HER2 Tyrosine Kinase Disintegrates Cancer Cell Membrane and Inhibits Tumor Growth In Vivo. Mol Cancer Ther. 2013; 12(4):384–393. [PubMed: 23358664]

55. Liu JB, Yu MX, Zhou C, Yang SY, Ning XH, Zheng J. Passive Tumor Targeting of Renal-Clearable Luminescent Gold Nanoparticles: Long Tumor Retention and Fast Normal Tissue Clearance. J Am Chem Soc. 2013; 135(13):4978–4981. [PubMed: 23506476]

56. Sancey L, Barbier E, Hirsjarvi S, et al. Enhanced Permeability and Retention (EPR) effect in tumors: characterization by MRI and fluorescence imaging. Bull Cancer (Paris). 2011; 98:S67–S67.

57. Li ML, Wang JC, Schwartz JA, Gill-Sharp KL, Stoica G, Wang LHV. In-vivo photoacoustic microscopy of nanoshell extravasation from solid tumor vasculature. J Biomed Opt. 2009; 14(1)

58. Paciotti GF, Myer L, Weinreich D, et al. Colloidal gold: A novel nanoparticle vector for tumor directed drug delivery. Drug Deliv. 2004; 11(3):169–183. [PubMed: 15204636]

59. Zhang XY, Hu WB, Li J, Tao L, Wei Y. A comparative study of cellular uptake and cytotoxicity of multi-walled carbon nanotubes, graphene oxide, and nanodiamond. Toxicol Res. 2012; 1(1):62–68.

60. Liu KK, Wang CC, Cheng CL, Chao JI. Endocytic carboxylated nanodiamond for the labeling and tracking of cell division and differentiation in cancer and stem cells. Biomaterials. 2009; 30(26): 4249–4259. [PubMed: 19500835]

61. Rojas S, Gispert JD, Martin R, et al. Biodistribution of Amino-Functionalized Diamond Nanoparticles In Vivo Studies Based on F-18 Radionuclide Emission. ACS Nano. 2011; 5(7): 5552–5559. [PubMed: 21657210]

62. Puzyr AP, Baron AV, Purtov KV, et al. Nanodiamonds with novel properties: A biological study. Diam Relat Mater. 2007; 16(12):2124–2128.

63. Yuan Y, Wang X, Jia G, et al. Pulmonary toxicity and translocation of nanodiamonds in mice. Diam Relat Mater. 2010; 19(4):291–299.

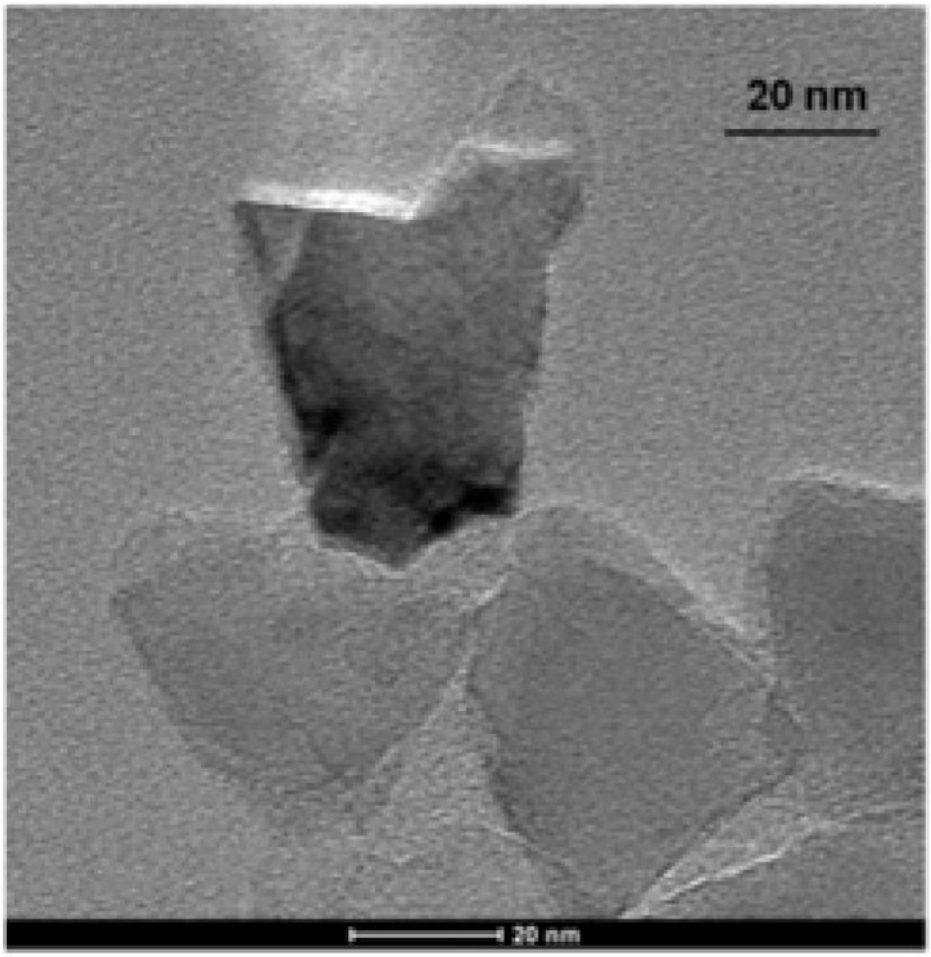

Figure 1.
TEM image of INDs.

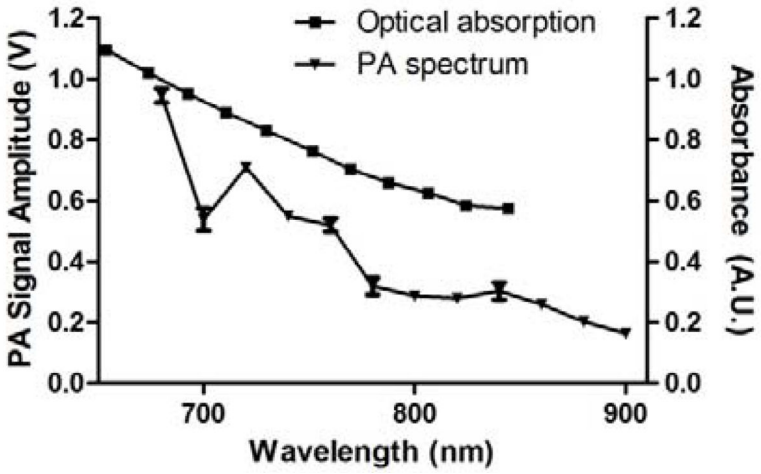

Figure 2.
Optical characteristics of INDs suspended in DI water as a function of wavelength.

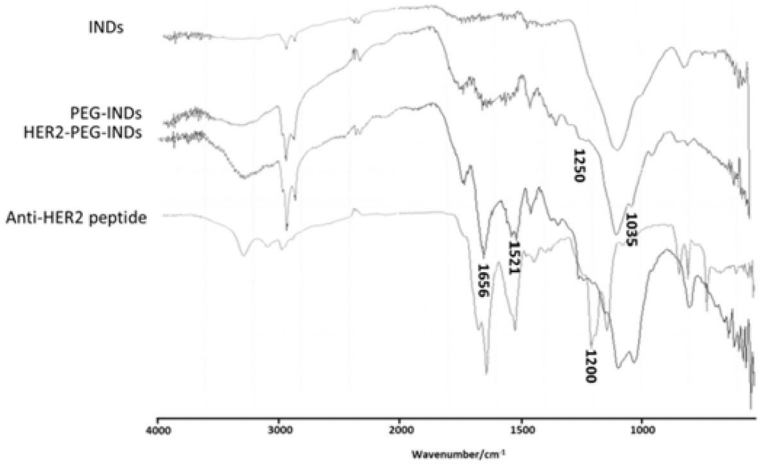

Figure 3.
Infrared spectra of IND, PEGylated INDs (PEG-INDs), HER2-PEGylated INDs (HER2-PEG-INDs) and anti-HER2 peptide.

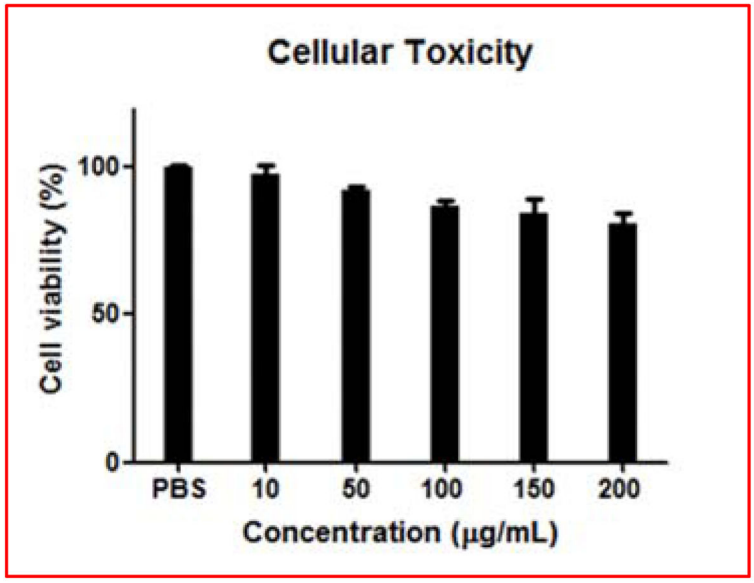

Figure 4.
Cytotoxicity evaluation on 4T1.2-neu cells after 48 h of incubation with HER2-PEG-INDs.

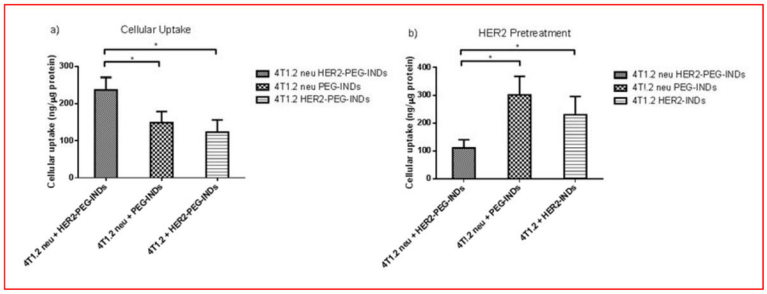

Figure 5.

Cellular uptake of INDs by 4T1.2 or 4T1.2-neu breast cencer cells without (a) and with (b) 0.75 μg/mL anti-HER2 peptide pretreatment (* $p < 0.05$).

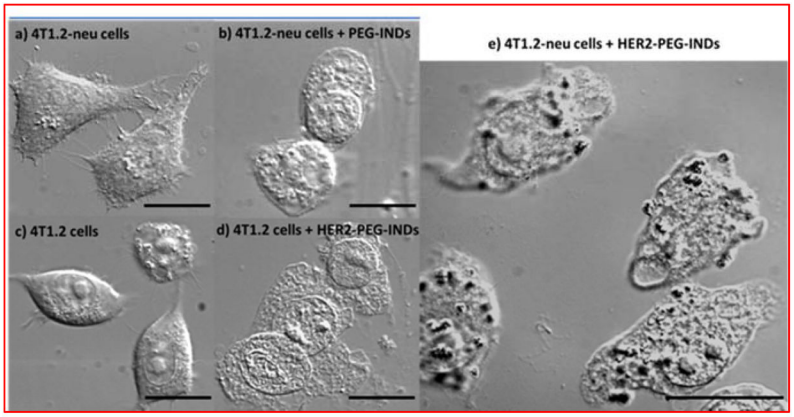

Figure 6.

Brightfield images of murine breast cancer cells. (a) Non-treated 4T1.2-neu cells, (b) 4T1.2-neu cells treated with PEG-INDs, (c) Non-treated 4T1.2 cells, (d) 4T1.2 cells treated with HER2-PEG-INDs and (e) 4T1.2-neu cells treated with HER2-PEG-INDs. Scale bars represent 10 μm in length.

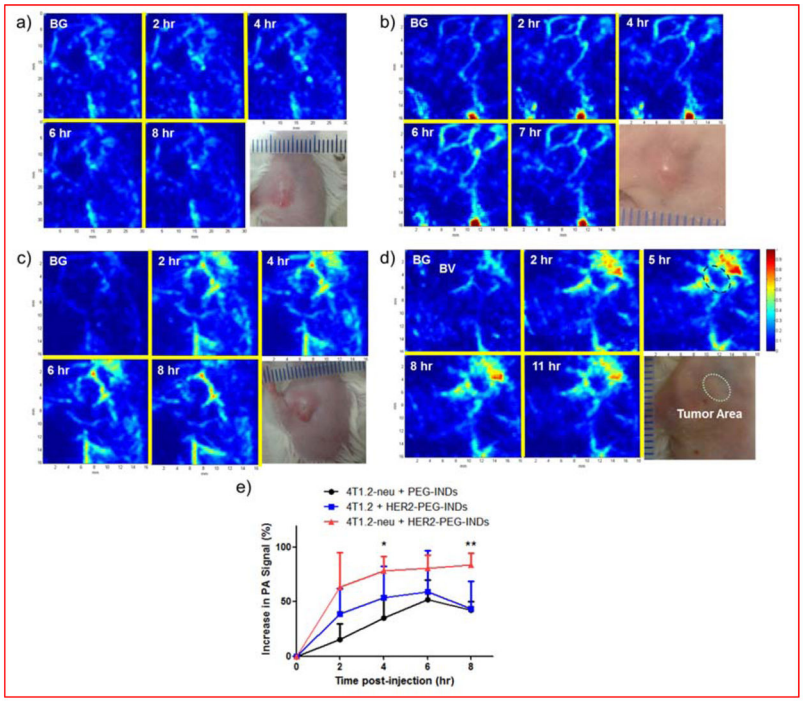

Figure 7.

PA images of ROI before and at different time points after the injection of saline or INDs and photographs of ROI. a) 4T1.2-neu tumor model injected with saline, b) 4T1.2-neu tumor model injected with PEG-INDs, c) 4T1.2 tumor model injected with HER2-PEG-INDs, d) 4T1.2-neu tumor model injected with HER2-PEG-INDs, e) increase in PA amplitude of tumor areas plotted as time post-injection (n=3, $p < 0.05$, * $p < 0.05$, ** $p < 0.01$).

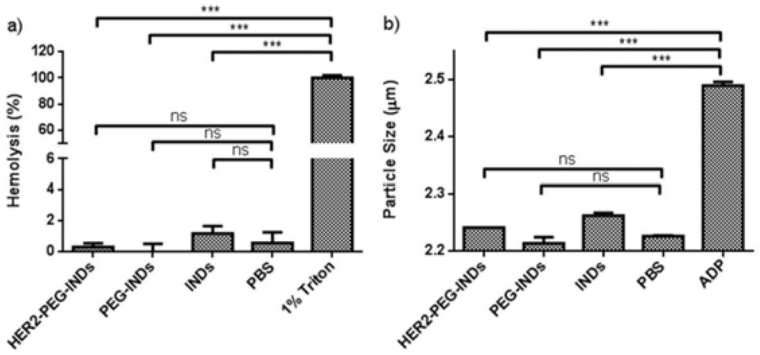

Figure 8.

Hemolysis and platelet coagulation studies of INDs with rat RBCs and PRP. a) hemolysis percentages measured for INDs incubated with RBCs at a concentration of 100 μg/mL, and b) Partical size of platelet aggregates measured for INDs incubated with PRP at a concentration of 100 μg/mL. The experiments were repeated in triplate (*** $p < 0.001$; ns, $p > 0.5$).

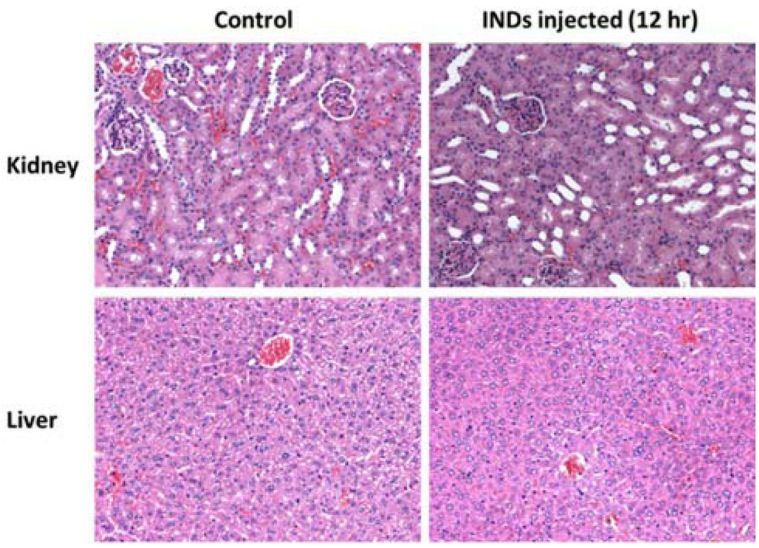

Figure 9.

Representative H&E stained images of kidneys and livers collected from saline injected mice and HER2-PEG-INDs injected mice at 12 hr post-injection.

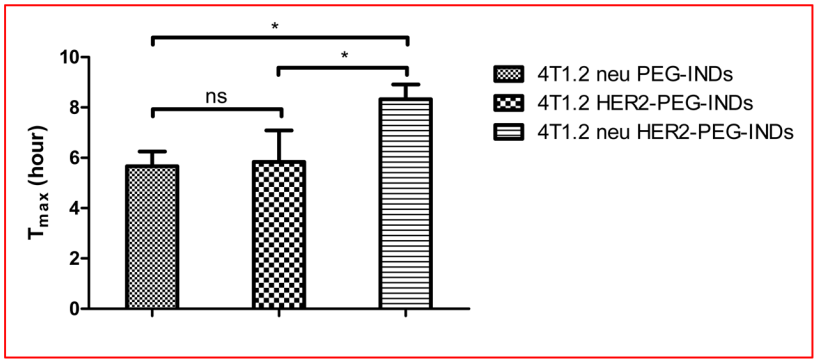

Figure 10.
Nanoparticle retention time in PA imaging groups (* $p < 0.05$; ns, $p > 0.05$).

Table 1

Particle sizes and zeta-potentials of INDs, PEGylated INDs and HER2 targeting peptide conjugated PEG-INDs.

Particles	Diameter (nm)	Zeta-potentials (mV)
INDs	38.3 ± 0.0	−36.49 ± 1.27
PEG-INDs	56.0 ± 0.1	−33.07 ± 1.44
HER2-PEG-INDs	92.1 ± 1.1	−22.67 ± 1.07